Acta Pharmaceutica Sinica B 2025;15(9):4886–4899

Chinese Pharmaceutical Association
Institute of Materia Medica, Chinese Academy of Medical Sciences

Acta Pharmaceutica Sinica B

www.elsevier.com/locate/apsb
www.sciencedirect.com



ORIGINAL ARTICLE

Activatable PROTAC nanoassembly for photodynamic PTP1B proteolysis enhances glioblastoma immunotherapy

Yeongji Jang[a,b,†], Jiwoong Choi[a,†], Byeongmin Park[a,c], Jung Yeon Park[c], Jae-Hyeon Lee[d], Jagyeong Goo[e], Dongwon Shin[a,c], Sun Hwa Kim[a,c], Yongju Kim[c,f], Hyun Kyu Song[b], Jooho Park[d], Kwangmeyung Kim[e,g,*], Yoosoo Yang[h,*], Man Kyu Shim[a,i,*]

[a]*Medicinal Materials Research Center, Biomedical Research Division, Korea Institute of Science and Technology (KIST), Seoul 02792, Republic of Korea*
[b]*Department of Life Sciences, Korea University, Seoul 02841, Republic of Korea*
[c]*KU-KIST Graduate School of Converging Science and Technology, Korea University, Seoul 02841, Republic of Korea*
[d]*Department of Applied Life Science, BK21 Program, Konkuk University, Chungju 27478, Republic of Korea*
[e]*College of Pharmacy, Graduate School of Pharmaceutical Sciences, Ewha Womans University, Seoul 03760, Republic of Korea*
[f]*Chemical and Biological Integrative Research Center, Korea Institute of Science and Technology, Seoul 02792, Republic of Korea*
[g]*Graduate Program in Innovative Biomaterials Convergence, Ewha Womans University, 52 Ewhayeodae-gil, Seodaemun-gu, Seoul 03760, Republic of Korea*
[h]*Department of Integrative Biotechnology, Sungkyunkwan University, Suwon 16419, Republic of Korea*
[i]*Division of Bio-Medical Science and Technology, KIST School, Korea University of Science and Technology, Seoul 02792, Republic of Korea*

Received 14 February 2025; received in revised form 18 March 2025; accepted 7 May 2025

*Corresponding authors.
E-mail addresses: kimkm@ewha.ac.kr (Kwangmeyung Kim), yangys@skku.edu (Yoosoo Yang), mks@kist.re.kr (Man Kyu Shim).
[†]These authors made equal contributions to this work.
Peer review under the responsibility of Chinese Pharmaceutical Association and Institute of Materia Medica, Chinese Academy of Medical Sciences.

https://doi.org/10.1016/j.apsb.2025.06.028
2211-3835 © 2025 The Authors. Published by Elsevier B.V. on behalf of Chinese Pharmaceutical Association and Institute of Materia Medica, Chinese Academy of Medical Sciences. This is an open access article under the CC BY-NC-ND license (http://creativecommons.org/licenses/by-nc-nd/4.0/).

KEY WORDS

Proteolysis-targeting chimera;
Targeted protein degradation;
Prodrug;
Supramolecular assembly;
Protein tyrosine phosphatase 1B;
Photodynamic therapy;
Nanomedicine;
Cancer immunotherapy

Abstract In light of the burgeoning successes of cancer immunotherapy, glioblastoma (GBM) remains refractory due to an immunosuppressive microenvironment originating from its molecular heterogeneity. Thus, identifying promising therapeutic targets for treating GBM and discovering methodologies to effectively regulate them is still a tremendous challenge. Here we describe photodynamic protein tyrosine phosphatase 1B (PTP1B) proteolysis mediated by a proteolysis-targeting chimera (PROTAC) nanoassembly. The PTP1B-targeting PROTAC is conjugated with a photosensitizer *via* a cathepsin B (Cat B)-cleavable peptide, which spontaneously forms nanoassemblies due to intermolecular π−π stacking interactions. In GBM models, PROTAC nanoassemblies significantly accumulate in the tumor region across the disrupted blood−brain barrier (BBB), triggering a burst release of the photosensitizer and active PROTAC by Cat B-mediated enzymatic cleavage. Upon laser irradiation, photodynamic therapy (PDT) synergizes with PROTAC-mediated PTP1B proteolysis to induce potent immunogenic cell death (ICD) in tumor cells. Subsequently, persistent PTP1B degradation by nanoassemblies in Cat B-overexpressed intratumoral T cells downregulates exhaustion markers, reinvigorating their functionality. These sequential processes of photodynamic PTP1B proteolysis ultimately augment T cell-mediated antitumor immunity as well as protective immunity, completely eradicating the primary GBM and preventing its recurrence. Overall, our findings underscore the therapeutic potential of combining PDT with PROTAC activity for GBM immunotherapy.

© 2025 The Authors. Published by Elsevier B.V. on behalf of Chinese Pharmaceutical Association and Institute of Materia Medica, Chinese Academy of Medical Sciences. This is an open access article under the CC BY-NC-ND license (http://creativecommons.org/licenses/by-nc-nd/4.0/).

1. Introduction

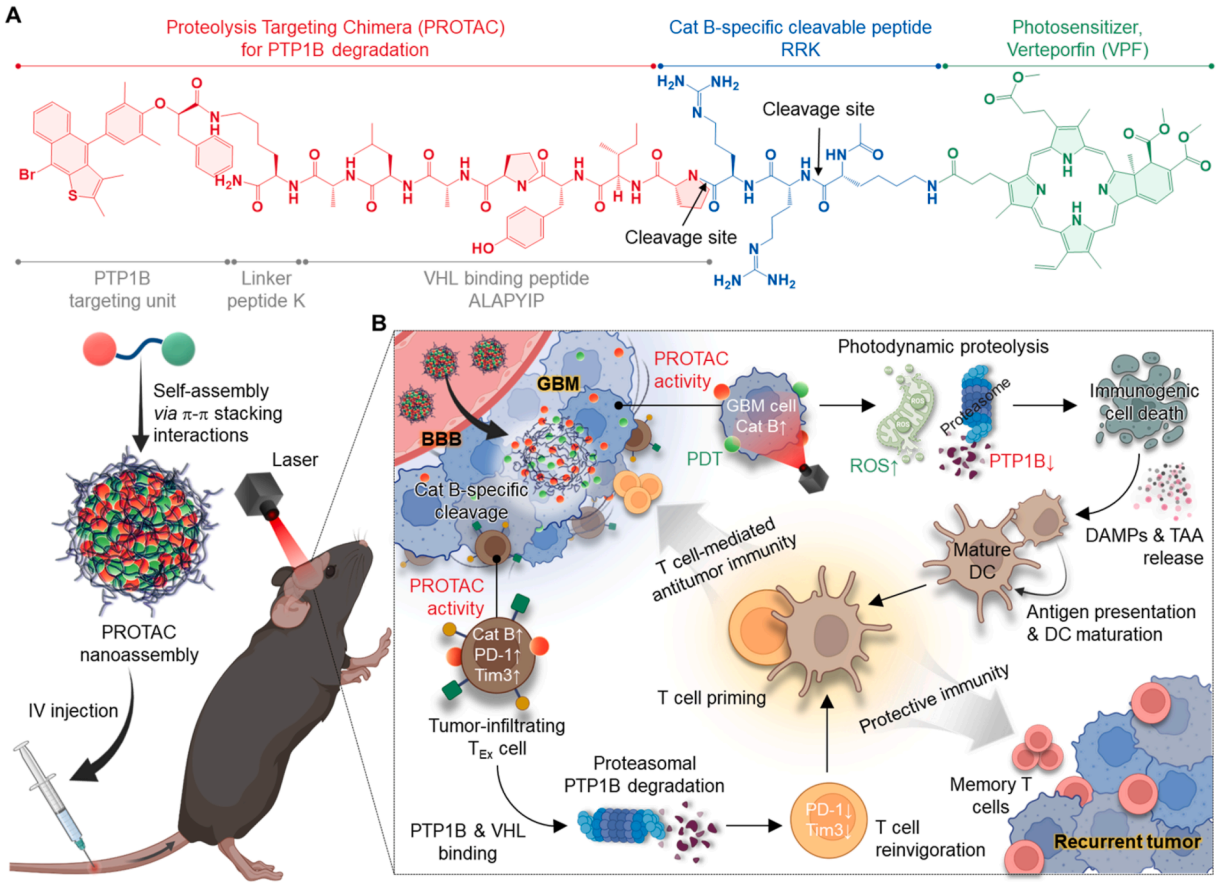
Glioblastoma (GBM) is recognized as the deadliest form of all primary malignancies, accounting for approximately 80% of central nervous system (CNS) tumors[1]. Mainstream therapies in clinical settings, such as chemotherapy and radiotherapy, have been ineffective for GBM, resulting in a growing effort to actively pursue the application of immunotherapy[2]. However, patients also exhibit a poor response to this therapeutic regimen due to the intrinsic heterogeneity of GBM, which is closely associated with an immunosuppressive tumor microenvironment (ITM)[3,4]. Among the several underlying mechanisms that compromise satisfactory outcomes, the main limiting factor is T cell exhaustion, characterized by overexpressed inhibitory receptors, reduced effector cytokine production and decreased cytolytic activity[5]. Therefore, unveiling key targets for reinvigorating exhausted T cells could become a central focus in designing effective immunotherapeutic strategies and represent a significant breakthrough in GBM treatment.

Protein tyrosine phosphatase 1B (PTP1B), well-known as a negative regulator of insulin and leptin signaling, has recently attracted renewed interest as a tumor promoter with specific roles depending on the cellular context[6]. Clinical data on the pathological characteristics of 136 patients have shown that PTP1B overexpression in GBM tissues contributes to tumorigenesis and is associated with a poor prognosis[7]. Additionally, PTP1B is also significantly upregulated in intratumoral T cells as an intracellular checkpoint, which limits their expansion and activity, ultimately resulting in immune cell exhaustion[8]. Together, these observations suggest that regulating PTP1B in tumor and immune cells within the GBM microenvironment can suppress tumor progression as well as restore T cell function. Various PTP1B inhibitors that can be utilized for this purpose are currently undergoing preclinical trials as antidiabetic agents, but these small molecule inhibitors struggle to sustain long-lasting effects in the ITM, which consistently maintains an immune-exclusive phenotype through several processes[9].

Proteolysis-targeting chimeras (PROTACs) are heterobifunctional molecules that bridge two ligands—one that binds to the protein of interest (POI) and the other to a ubiquitin ligase—*via* a linker[10]. Relative to small molecule inhibitors, PROTACs are capable of inducing the irreversible targeted protein degradation (TPD) of pharmaceutically undruggable POIs with persistent and recyclable action[11]. Hence, various PROTAC candidates have been developed to eliminate a range of oncogenic proteins, with some advancing to industry. For instance, ARV-110 and ARV-471 are currently in phase II and III trials for prostate and breast cancer patients by targeting the androgen receptor and estrogen receptor, respectively[12,13]. In particular, many attempts are being made to apply this technology to immunotherapy, including PTP1B-targeting PROTACs for T cell activation[14]. However, off-target side effects in accordance with the always-on bioactivity of PROTACs remain a critical bottleneck for clinical use, making the improvement of therapeutic specificity essential[15].

We herein propose a PROTAC nanoassembly eliciting photodynamic PTP1B proteolysis (PN_{PTP1B}) for GBM immunotherapy. The PTP1B-targeting PROTAC is linked to a photosensitizer through a cathepsin B (Cat B)-cleavable peptide, spontaneously self-assembling into nanoparticles *via* intermolecular π−π stacking interactions (Scheme 1A)[16-18]. By omitting the excessive carrier materials used in conventional nanoparticle systems, these nanoassemblies accomplish over 80% drug loading capacity and minimize the adverse events associated with such materials[19,20]. From an industrial perspective, its well-defined chemical structure is highly amenable to quality control (QC) and mass production, similar to small molecule drugs, potentially addressing the fundamental challenges faced in the clinical translation of traditional nanoparticles[21].

Following intravenous injection in a GBM model, PN_{PTP1B} accumulates in the target region by crossing the disrupted blood−brain barrier (BBB) during disease progression, subsequently decomposing into photosensitizers and active PROTACs through enzymatic cleavage by the biomarker Cat B (Scheme 1B)[22]. The BBB in GBM allows the passive accumulation of



Scheme 1 The structure of PN_{PTP1B} and its mode of action for photodynamic PTP1B proteolysis in GBM immunotherapy. (A) The prodrug conjugate, which consists of a PTP1B-targeting PROTAC, a cathepsin B (Cat B)-cleavable RRK peptide and the photosensitizer verteporfin (VPF), forming PN_{PTP1B} *via* intermolecular $\pi-\pi$ stacking interactions. Both ends of RR in the prodrug are cleaved by cathepsin B, releasing PROTAC and K-conjugated VPF. (B) The cascade events of photodynamic PTP1B proteolysis for GBM immunotherapy. PN_{PTP1B} accumulates significantly within the GBM region across the disrupted BBB, decomposing into VPF and active PROTACs due to enzymatic cleavage mediated by the biomarker Cat-B. Upon laser irradiation, the combination of photodynamic therapy (PDT) and PTP1B proteolysis by PROTAC induces potent immunogenic cell death in tumor cells, leading to DC maturation and T cell priming. Thereafter, PN_{PTP1B} persistently counteracts intratumoral T cell exhaustion in the GBM microenvironment by downregulating PD-1 and Tim3 through the recyclable action of PROTAC. Ultimately, such photodynamic PTP1B proteolysis triggered by PN_{PTP1B} enhances T cell-mediated antitumor immunity as well as protective immunity, eradicating GBM and preventing its recurrence.

10−100 nm-sized particles due to increased vascular permeability, resulting from diminished tight junctions, irregular pericyte coverage and the presence of stem cell-derived pericytes[23,24]. Additionally, nanoparticles preferentially accumulate in GBM *via* the enhanced permeability and retention (EPR) effect, driven by leaky vasculature and impaired lymphatic drainage in the tumor microenvironment[25-28]. Upon laser irradiation, reactive oxygen species (ROS) generated by the photosensitizer verteporfin (VPF), combined with PROTAC-mediated *PTP1B* knockdown, which contributes to cancer cell death through the PKM2/AMPK/mTORC1 signaling pathways[29-31], synergistically trigger immunogenic cell death (ICD) in GBM cells. Photodynamic therapy (PDT) induces endoplasmic reticulum (ER) stress-mediated ICD, and its synergy with TPD effectively promotes the release of damage-associated molecular patterns (DAMPs) and tumor-associated antigens (TAAs) from tumor cells, driving dendritic cell (DC) maturation and T cell priming[32-34]. Thereafter, PN_{PTP1B} also improves the short-lived lytic activity of T cells in the GBM microenvironment by downregulating exhaustion markers programmed cell death protein 1 (PD-1) and T-cell immunoglobulin and mucin domain 3 (Tim3) in Cat B-overexpressed intratumoral T cells *via* PTP1B proteolysis. The inherent recyclable action of PROTACs persistently counteracts T cell exhaustion, thereby enhancing T cell-mediated antitumor immunity for the complete regression of GBM and establishing protective immunity to prevent recurrence. This study highlights the superior immunotherapy efficacy of photodynamic PTP1B proteolysis, which reshapes the immunosuppressive network in GBM.

2. Materials and methods

2.1. *Synthesis of PN_{PTP1B}*

Initially, VPF (274 mg, 0.38 mmol, Frontier Scientific) and the C-terminal aminated K (Fmoc) ALAPYIPRRK N-terminal acetylated peptide (600 mg, 0.38 mmol, Peptron) were linked *via* amide condensation in the presence of *N*-hydroxysuccinimide (NHS, 72 mg, 1.9 mmol, Sigma−Aldrich) and 1-ethyl-3-(3-

dimethylaminopropyl) carbodiimide (EDC, 120 mg, 1.9 mmol, Sigma−Aldrich). After a 6 h reaction, VPF-K (Fmoc) ALAPYIPRRK was purified using a Sep-Pak® C18 6 cc Vac cartridge (Waters) to remove any unreacted substances, followed by incubation in anhydrous DMF containing 20% (*v*/*v*) piperidine for Fmoc deprotection. Finally, the resulting VPF-KALAPYIPRRK (536 mg, 0.26 mmol) was reacted with ertiprotafib (145 mg, 0.26 mmol, MedChemExpress) in anhydrous DMF through the EDC (250 mg, 1.3 mmol)/NHS (150 mg, 1.3 mmol) amide coupling reaction for 2 h. The final product, VPF−KALAPYIPRRK−ertiprotafib, was purified using the same protocol as described above. The control PROTAC compound was prepared by reacting the N-terminal acetylated and C-terminal amidated KALAPYIP peptide (238.5 mg, 0.26 mmol) with ertiprotafib (145 mg, 0.26 mmol) in the presence of NHS (150 mg, 1.3 mmol) and EDC (250 mg, 1.3 mmol), followed by purification using LC−MS. Throughout the synthesis process, the purity and molecular weights of all intermediate compounds and the final product were analyzed using LC−MS (Agilent Technology).

2.2. Physicochemical characterization

The prepared prodrug conjugates self-assembled into nanoparticles through $\pi-\pi$ interactions induced by VPF when exposed to aqueous conditions, without the need for any additional carrier material-related formulation process[16]. The hydrodynamic size and morphology of PN_{PTP1B} in saline (1 mg/mL) were examined using dynamic light scattering (DLS, Zetasizer Nano ZS, Malvern Instruments) and transmission electron microscopy (CM-200 Series, Philips), respectively. The drug loading capacity was determined based on the following formula: the sum of the molecular weights of PROTAC (1411.59 *m*/*z*) and VPF (702.81 *m*/*z*), excluding the cathepsin B-cleavable RRK peptide (464.61 *m*/*z*)/the molecular weight of the whole prodrug conjugate (2595.98 *m*/*z*). The UV−vis absorbance and fluorescence spectrum were monitored using a UV spectrophotometer and a fluorescence spectrophotometer, respectively. To evaluate the target enzyme-specific cleavage, PN_{PTP1B} was incubated in a pH 5.5 MES buffer at 37 °C with 10 μg/mL of Cat B (R&D Systems), and its irreversible inhibitor Z-FA-FMK (MedChemExpress), Cat D (R&D Systems), Cat E (R&D Systems), Cat L (R&D Systems), caspase-3 (R&D Systems) or MMP-9 (R&D Systems), followed by HPLC analysis[35,36].

2.3. Molecular simulations

The molecular structure of PTP1B-targeting PROTAC was illustrated using Chemdraw Professional 20.1.1.125 (PerkinElmer Inc.). Molecular docking was performed with the AMDock (Assisted Molecular Docking) software against the PTP1B and VHL proteins (PDB: 1QXK, 1LM8), utilizing the CHARMm (Chemistry at Harvard Molecule Mechanics) force field. The binding site was identified based on the active site of the ligand by referring to the existing references[37,38,40]. After the docking process, the 2D diagram interaction analysis was performed using Discovery Studio 2022 (v22.1.0.) software (BIOVIA; CA, USA). The optimized molecular conformations were visualized using PyMOL.

2.4. In vitro cellular uptake, ROS generation and cytotoxicity

Murine glioblastoma cell line GL261 cells (American Type Culture Collection, ATCC) seeded in confocal dishes were treated with 5 μmol/L PN_{PTP1B} or VPF. The cells were then washed twice with DPBS, incubated with 4% paraformaldehyde (Biosesang) for 20 min, stained with DAPI for 15 min and imaged using a confocal laser scanning microscopy (Leica Microsystems). For the analysis of ROS generation, GL261 cells treated with 5 μmol/L PN_{PTP1B} or VPF for 24 h were further incubated with dichlorodihydro-fluorescein diacetate (DCFH-DA, Sigma−Aldrich) for 30 min, followed by exposure to laser irradiation at 40 mW for 500 s. For the cytotoxicity study, GL261 cells seeded in a 96-well cell culture plate were treated with PN_{PTP1B} or ertiprotafib for 24 h. Cell viability was determined using a microplate reader at 450 nm UV−vis wavelength (VERSAmax, Molecular Devices Corporation) after the cells were incubated with a medium containing 10% CCK-8 solution (DOJINDO) for 20 min.

2.5. In vitro PTP1B proteolysis

2×10^5 GL261 cells seeded in confocal dishes were incubated with IFN-γ for 12 h and then treated with 5 μmol/L PN_{PTP1B} for 24 h. Subsequently, the cells were incubated with a rabbit monoclonal anti-PTP1B antibody (Abcam) overnight at 4 °C, followed by additional incubation with Alexa Fluor 488-conjugated anti-rabbit IgG (Thermo Fisher Scientific) for 1 h. GL261 cells were pretreated with CA-074-Me (MedchemExpress), pevonedistat (MedchemExpress) or epoxomicin (MedchemExpress) for 6 h before PN_{PTP1B} treatment. Intracellular PTP1B expression was imaged using confocal laser scanning microscopy.

To investigate the changes in intracellular proteins associated with PTP1B degradation, a Western blot was performed after the GL261 cells, treated with the same protocol as described above, were lysed using RIPA buffer supplemented with 1% protease/phosphatase inhibitor cocktail (Thermo Fisher Scientific). Following protein quantification using a BCA assay kit (Thermo Fisher Scientific), equal amounts of proteins were separated on a 10% sodium dodecyl sulfate-polyacrylamide gel *via* electrophoresis for 90 min at 100 V and subsequently transferred onto polyvinylidene fluoride membranes. The membranes were incubated with 5% skim milk for 1 h to prevent non-specific IgG binding, then with the primary antibodies overnight at 4 °C and finally with the appropriate secondary antibodies for 1 h at room temperature. The antibodies used in this study were as follows: PTP1B (Abcam), phospho-Akt (Cell Signaling Technology), Akt (Cell Signaling Technology), phospho-p44/42 MAPK (Erk1/2; Cell Signaling Technology), p44/42 MAPK (Erk1/2; Cell Signaling Technology), GAPDH (GeneTex), anti-rabbit IgG-HRP antibody (GeneTex) and anti-mouse IgG-HRP antibody (GeneTex). The protein signals were visualized using ECL substrate (Bio-Rad) and detected with iBright Imaging Systems (Invitrogen).

2.6. In vitro DAMP analysis

GL261 cells, treated with 5 μmol/L ertiprotafib or PN_{PTP1B} (without or with laser irradiation at 40 mW power for 500 s) for 24 h, were stained with an anti-CRT antibody (Alexa Fluor 488, Abcam). All samples were analyzed using a CytoFLEX flow cytometer (Beckman Coulter) and plotted using FlowJo (v10) software. Meanwhile, HMGB1 (Abcam) and HSP70 (Abcam) in the culture medium were assessed through Western blot, and ATP (Beyotime Biotechnology) was quantified by an ELISA assay.

2.7. T cell isolation and culture

The animal studies were conducted in accordance with the relevant laws and institutional guidelines of the Institutional Animal Care and Use Committee at the Korea Institute of Science and Technology (approval number: 2023-013). The mice were purchased from OrientBio and bred under pathogen-free conditions at KIST. To establish the GBM model, 5×10^6 GL261 cells suspended in DMEM media were subcutaneously inoculated into the left flank of C57BL/6 mice. Intratumoral $CD8^+$ T cells were isolated using $CD8^+$ Microbeads (Miltenyi Biotec) according to the manufacturer's instructions and maintained in RPMI1640 media supplemented with 10% fetal bovine serum (Gibco) and 1% antibiotics (Gibco) at 5% CO_2 and 37 °C. The splenic $CD8^+$ T cells were obtained from tumor-baring or naive mice using the same protocol as above.

2.8. T cell proliferation and coculture assays

The expression levels of PTP1B, PD-1 and Tim3 in intratumoral $CD8^+$ T cells, treated with 5 μmol/L PN_{PTP1B} or ertiprotafib for 24 or 48 h, were analyzed *via* Western blot using relevant antibodies (PTP1B from Abcam, PD-1 and Tim3 from Biolegend) and the same protocol as described above. For proliferation assay, intratumoral $CD8^+$ T cells were stained with the CellTrace™ CFSE Cell Proliferation Kit (Invitrogen) and treated with 5 μmol/L PN_{PTP1B} or ertiprotafib for 48 h. The decreased CFSE fluorescence intensity of daughter T cells was compared to that of parental cells following cell division. To evaluate enhanced T cell activity, green CFSE-stained GL261 cells were cocultured for 1 h with Far red CFSE-stained intratumoral T cells treated with 5 μmol/L PN_{PTP1B} or ertiprotafib for 48 h. The lysis of tumor cells by T cells was examined by measuring the viability of GL261 cells using the CCK-8 assay.

2.9. Biodistribution and antitumor immune responses

The biodistribution of PN_{PTP1B} was evaluated in six-week-old female BALB/c-*nu* mice to avoid fluorescence interference. GBM models were intravenously injected with VPF or PN_{PTP1B} based on an equivalent 3 mg/kg VPF content when tumor volumes reached approximately 50 mm^3, followed by *in vivo* and *ex vivo* NIRF imaging using an IVIS Lumina Series III (PerkinElmer). Fluorescence intensities in the NIRF images were calculated using LivingImage software (PerkinElmer).

Therapeutic efficacy and antitumor immune responses were assessed in six-week-old female C57BL/6 mice. GBM models were divided into five groups: (i) saline, (ii) laser only (Laser), (iii) PROTAC, (iv) VPF with laser irradiation (+L), (v) PN_{PTP1B} without laser irradiation (-L) and (vi) PN_{PTP1B} (+L). Following the intravenous injection of VPF or PN_{PTP1B} based on an equivalent 3 mg/kg VPF content, the tumor tissues were exposed to laser irradiation at 100 mW for 15 min after 3 h of treatment. A 671 nm wavelength laser (SDL-671 series, Shanghai Dream Laser Technology Co., Ltd., China), which efficiently penetrates the mouse skull with an average thickness of 0.34 ± 0.05 mm, was used for PDT[39]. The control PROTAC compound was administered with equal PROTAC content as PN_{PTP1B}. Tumor growth was monitored by measuring tumor volumes using Eq. (1):

$$\text{Tumor growth} = \text{Largest diameter} \times \text{Smallest diameter}^2 \times 0.53 \quad (1)$$

Mice with tumor volumes exceeding 1000 mm^3 were considered dead.

For the immune cell analysis, single cells were initially isolated from the tumor tissues collected from the GBM model on Day 3 using a tumor dissociation kit (Miltenyi Biotechnology). The cells were then incubated with FcBlock (Cell Signaling Technology) for 5 min, followed by staining with appropriate antibodies for 45 min to analyze the following populations: (i) CRT-positive tumor cells ($CD45^-CRT^+$), (ii) exhausted T cells ($CD3^+CD8^+PD\text{-}1^+$), (iii) mature dendritic cells ($CD11c^+CD40^+$), (iv) cytotoxic T cells ($CD45^+CD3^+CD8^+$) and (v) damaged T cells ($CD8^+$Annexin V^+). The levels of HMGB1 and HSP70 in supernatants were quantified *via* Western blot. IFN-γ concentrations were measured using an ELISA assay kit (R&D Systems).

GBM mice that experienced complete tumor regression following treatment with PN_{PTP1B} (+L) were further inoculated with 5×10^6 GL261 cells *via* subcutaneous injection. Rechallenged tumor volumes were calculated every two days. On Day 15 after the tumor rechallenge, the splenic effector memory $CD8^+$ T cells (T_{em}; $CD3^+CD8^+CD44^+CD62L^{low}$) was assessed using a flow cytometer. Serum levels of IL-6 (R&D Systems) and IFN-γ were quantified using ELISA assay kits.

2.10. Therapeutic efficacy in orthotopic GBM model

To establish an orthotopic GBM model, GL261 cells were injected into the brains of BALB/c-*nu* and C57BL/6 mice, which were used to evaluate biodistribution and therapeutic efficacy, respectively. Briefly, the mice were secured with ear bars in a stereotactic device (Stoelting Co.). Next, 1×10^5 GL261 cells suspended in 8 μL of saline were drawn into a 26-gauge Hamilton syringe. A precise hole was drilled in the skull at coordinates 2.0 mm lateral and 0.5 mm anterior to the bregma. Through this hole, the needle was placed at a depth of 3.0 mm, and the cells were inoculated at a regulated flow rate of 1 μL/min. After a 5 min waiting period to prevent leakage, the syringe was gradually withdrawn over another 5 min. The *in vivo* brain accumulation of VPF and PN_{PTP1B} was monitored using an IVIS Lumina Series III. Therapeutic efficacy was assessed in orthotopic GBM models with four groups: (i) Sham, (ii) Laser, (iii) VPF (+L) and (iv) PN_{PTP1B} (+L), following treatment with the same protocol as described above. Unlike the flank GBM model, which was exposed to laser irradiation 3 h after intravenous administration, laser irradiation was performed in the brains of the orthotopic GBM model at 6 h post-injection, when the highest tumor accumulation of PN_{PTP1B} was observed. Three days following treatment, brain tissues were collected for staining with TUNEL (PROMEGA), CD8, PTP1B, PD-1 and Tim3. H&E staining was conducted on Day 10 after treatment.

2.11. Statistics

Statistical significance between the two groups was assessed using the Student's *t*-test. For comparisons involving more than two groups, a one-way analysis of variance (ANOVA) was conducted, followed by multiple comparisons using the Tukey−Kramer *post hoc* test. Survival outcomes were plotted using Kaplan−Meier curves and analyzed with the log-rank test. All results are expressed as mean ± standard deviation (SD), with *P* values of $>0.05^{ns}$, <0.05*, <0.01**, <0.001*** and <0.0001****.

3. Results and discussion

3.1. Synthesis and physicochemical characterization

PN_{PTP1B} was derived from the self-assembly of prodrug conjugates, which were synthesized as shown in Supporting Information Fig. S1. The photosensitizer VPF was first reacted with a K (Fmoc) ALAPYIPRRK peptide through an amine group in the K sequence. Following Fmoc deprotection, KALAPYIPRRK−VPF was conjugated with ertiprotafib *via* an amide condensation, resulting in the prodrug conjugate. The successful synthesis of all intermediates and the final product was verified by LC−MS analysis (Supporting Information Fig. S2). Ultimately, this conjugate is a tripartite structure, with each component having a unique function: (i) a PROTAC for the degradation of PTP1B, (ii) a Cat B-specific cleavable KRR sequence[40] and (iii) the clinically approved VPF, marketed under the trade name Visudyne, as a photosensitizer[41]. The PROTAC features ertiprotafib and the ALAPYIP peptide to target PTP1B and E3 ubiquitin ligase VHL, respectively, linked through the K sequence. A previous study has demonstrated that the K sequence can serve as a linker for PROTAC by providing a short carbon chain[42]. Ertiprotafib belongs to a novel class of PTP1B-selective inhibitors that have reached clinical trials for the treatment of diabetes[43].

Prodrug conjugates spontaneously self-assembled under aqueous conditions, exhibiting uniform size distribution and spherical morphology with an average diameter of 87.79 ± 1.25 nm (Fig. 1A). The driving force behind the self-assembly of the system was visualized by molecular dynamics (MD) simulations, which revealed that four prodrug molecules are maintained in close proximity due to π−π interactions between the aromatic segments of VPF (Fig. 1B and Supporting Information Fig. S3). MD simulations further confirmed that removing VPF from the prodrug conjugates fails to promote the self-assembly of molecules (Supporting Information Fig. S4). Additionally, the radius of gyration (ROG) of the prodrug tetramer gradually decreased over the simulation time due to the compacting of the assembled structure into aggregates (Fig. 1C). In contrast, no decrease in ROG was observed when VPF was absent from the structure. These results indicate that prodrug conjugates form nanoassemblies solely *via* intermolecular interactions without the use of additional carrier materials. The interaction between the PROTAC cleaved from the prodrug conjugate and the two target proteins (PTP1B and VHL) was further simulated to confirm the binding ability. As illustrated in Supporting Information Fig. S5, the ertiprotafib moiety in PROTAC forms an extensive binding network with the catalytic site of PTP1B, incorporating electrostatic and hydrogen bond networks. Notably, the fused aromatic rings exhibit cation−π interactions with Lys116, while also showing potential interactions with π−alkyl and alkyl hydrophobic residues. Furthermore, the ertiprotafib engages in additional interactions, including conventional hydrogen bonds and carbon−hydrogen bonds with Gly183, Pro180, Asp181 and Arg112. Additionally, the AVPIAQ peptide sequence in PROTAC interacts with VHL, forming hydrogen bonds, π−alkyl interactions and van der Waals interactions. In particular, His110, Ile109 and Tyr112 exhibit the potential to form conventional hydrogen bonds, while Trp88 and His115 are expected to contribute additional binding affinity through π−alkyl interactions. Pro99 and Trp117 may enhance molecular accommodation within the binding site through van der Waals interactions.

The resulting PN_{PTP1B} achieves an outstanding drug loading capacity of 88.6% comprising 54.4% PROTAC and 34.2% VPF. The nanoassemblies demonstrated remarkable stability in mouse serum, showing no significant changes in hydrodynamic size and polydispersity index (PDI) for 3 days (Fig. 1D and Supporting Information Table S1). The UV−vis spectrum of PN_{PTP1B} displayed characteristic absorption peaks at approximately 370, 430, 580, 630 and 690 nm (Fig. 1E and Supporting Information Fig. S6). Both PN_{PTP1B} and VPF revealed similar fluorescence emissions, peaking at 670 nm (Fig. 1F). The PN_{PTP1B} and VPF promoted comparable levels of ROS upon laser irradiation, suggesting that the photoactivity of VPF remains unaltered following its modification into prodrug conjugates (Fig. 1G). Lastly, PN_{PTP1B} was completely cleaved into PROTAC and K-conjugated VPF (VPF−K) within 1 h incubation with Cat B (Fig. 1H). LC−MS analysis supported these findings by identifying the exact molecular weights corresponding to each metabolite (1412.2 *m/z* [M] and 706.2 $[M+2H]^{2+}$ for PROTAC, 888.6 *m/z* [M] for VPF−K; Supporting Information Fig. S7). In contrast, no detectable enzymatic cleavage was observed when incubated with Cat B and its inhibitor Z−FA−FMK. The nanoassemblies were also stable in the presence of enzymes other than Cat B, such as Cat D, Cat E, Cat L, caspase-3 or MMP-9, demonstrating superior selectivity towards the target biomarker (Fig. 1I).

3.2. In vitro evaluation of photodynamic PTP1B proteolysis

Considering that GBM exhibits elevated levels and activity of Cat B associated with tumor progression[22], the photodynamic PTP1B proteolysis by PN_{PTP1B} was investigated in the mouse glioma cell line GL261. Their cellular uptake gradually increased in a time-dependent manner, plateauing after 24 h of incubation, which was slightly delayed compared to VPF (Fig. 2A and Supporting Information Fig. S8). The levels of intracellular ROS generated by PN_{PTP1B} and VPF were nearly identical when the cells were exposed to laser irradiation after both compounds reached maximal uptake at 24 h post-incubation (Fig. 2B). In contrast, no ROS generation was detected in cells treated with only PN_{PTP1B} or VPF in the absence of laser irradiation.

To verify *in vitro* PROTAC activity, we evaluated the degradation of PTP1B and changes in the related downstream signaling pathways, due to treatment with PN_{PTP1B}. PTP1B contributes to GBM progression *via* the Src/ERK and PI3K/AKT pathways by phosphorylating the ERK and AKT proteins[29]. GL261 cells significantly upregulated PTP1B expression, accompanied by an increase in phosphorylated ERK (pERK) and AKT (pAKT), after incubation with IFN-γ (Fig. 2C and Supporting Information Fig. S9). Subsequent treatment with PN_{PTP1B} noticeably degraded the target protein in a concentration-dependent manner and also reduced the levels of pERK and pAKT. Notably, PTP1B and related downstream proteins were fully restored to levels similar to those in IFN-γ-untreated cells after treatment with 5 μmol/L PN_{PTP1B}. As a control, IFN-γ-treated cells experienced only a decrease in pERK and pAKT with no changes in PTP1B levels following incubation with the allosteric inhibitor ertiprotafib (Supporting Information Fig. S10). Therefore, these findings demonstrate the PROTAC-mediated TPD by PN_{PTP1B}, which directly removes PTP1B. Importantly, PROTAC activity of PN_{PTP1B} more effectively downregulated pERK and pAKT compared to an equivalent concentration of ertiprotafib; indeed, high concentrations of nanoassemblies decreased these oncogenic proteins to levels comparable to those in untreated cells. The PROTAC activity of

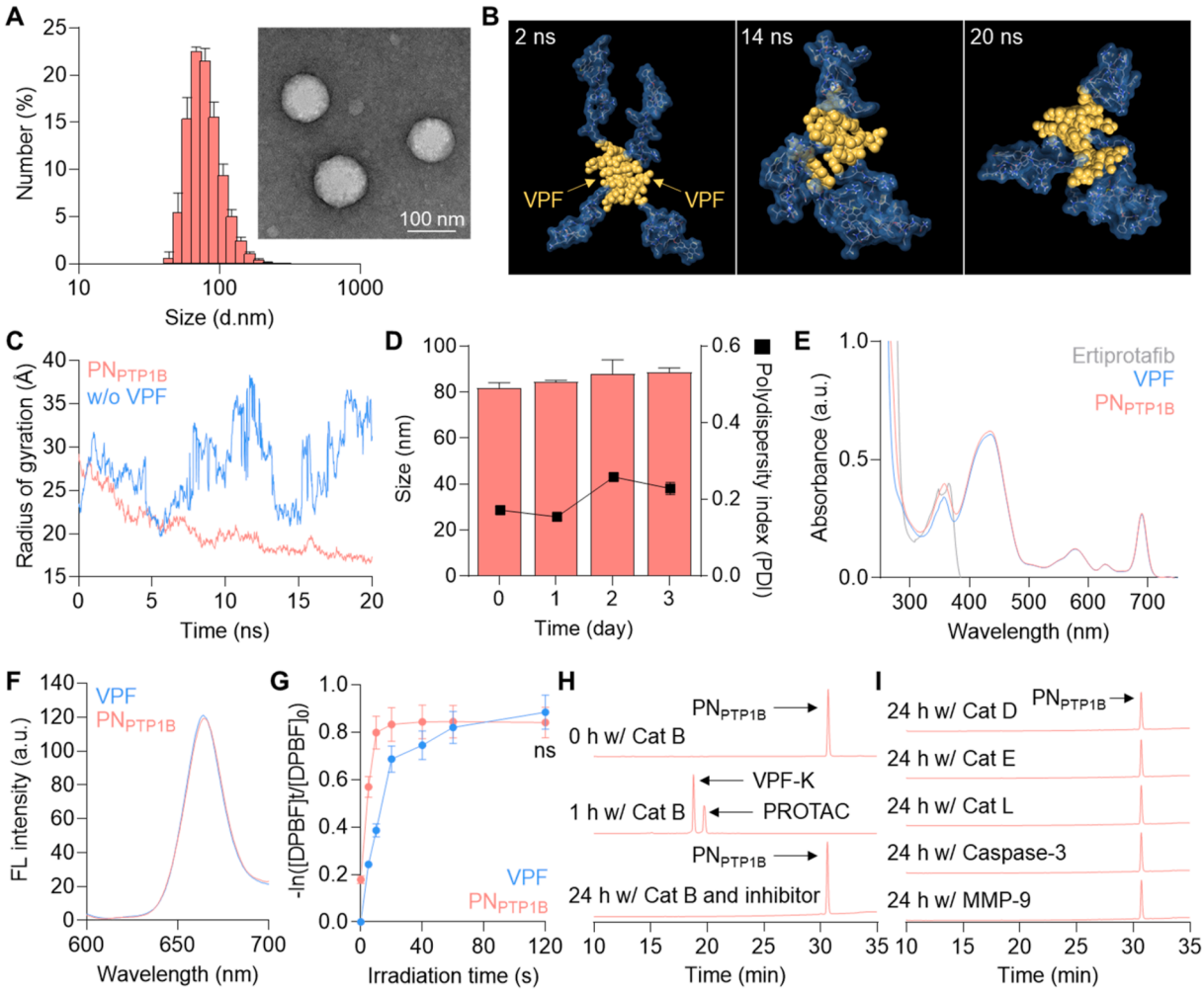


Figure 1 Physicochemical characterization of PN_{PTP1B}. (A) Hydrodynamic size and morphology of PN_{PTP1B} in aqueous condition ($n = 5$). (B) Molecular dynamics (MD) simulation of prodrug tetramer, with the aromatic segments of VPF highlighted in yellow for clarity. (C) Radius of gyration (ROG) spectrum determined from MD simulation results over 20 ns. (D) Average particle size and polydispersity index (PDI) of PN_{PTP1B} in mouse serum ($n = 5$). (E) UV−vis and (F) fluorescence spectra of PN_{PTP1B} and VPF. (G) ROS generation by PN_{PTP1B} and VPF under laser irradiation ($n = 5$). Cleavage behavior of PN_{PTP1B} upon incubation in (H) Cat B alone or with its inhibitor, or (I) other enzymes such as Cat D, Cat E, Cat L, caspase-3 and MMP-9.

PN_{PTP1B} was significantly suppressed by pretreatment with various inhibitors, such as a Cat B inhibitor (CA-074-Me), a neddylation inhibitor (NEDD8-activating enzyme inhibitor; Pevonedistat) or a 20S proteasome inhibitor (epoxomicin; Fig. 2D and Supporting Information Fig. S11). From these results, the mechanism of PTP1B proteolysis of PN_{PTP1B} was identified as follows: in the presence of Cat B, nanoassemblies are first decomposed to active PROTAC, which binds to PTP1B and subsequently brings the E3 ligase. The E3 ligase is then activated by the NEDD8-activating enzyme to induce polyubiquitination of PTP1B and recruit the proteasome for degradation, ultimately leading to downregulation of the Src/ERK and PI3K/AKT pathways. Therefore, PN_{PTP1B} can mitigate uncontrolled proteolysis at off-target sites by silencing the always-on bioactivity of PROTAC and selectively stimulating it only in the presence of the target enzyme.

The cytotoxicity of PN_{PTP1B}-mediated photodynamic PTP1B proteolysis was evaluated under cultured conditions. Allosteric inhibition of PTP1B with ertiprotafib resulted in minimum GBM cell death (Fig. 2E). Interestingly, PN_{PTP1B} without laser irradiation (-L) elicited significantly greater cytotoxicity than ertiprotafib, highlighting the superior efficacy of PTP1B proteolysis over the conformational blockade. Upon laser irradiation (+L), the nanoassemblies exhibited an even more potent tumor-killing effect. In addition, surface calreticulin (CRT) and the extracellular release of high-mobility group box 1 (HMGB1), heat shock protein 70 (HSP70) and ATP were significantly increased in GL261 cells treated with PN_{PTP1B} under laser irradiation (Fig. 2F and G, Supporting Information Fig. S12). Notably, inhibition of PTP1B using PN_{PTP1B} (-L) was shown to slightly induce the release of DAMPs in GL261 cells, suggesting that PTP1B might influence the ER stress response, autophagy or other processes intersecting with the pathways driving ICD. These findings verify that PN_{PTP1B} synergizes photoactivity and the PROTAC mode of action to promote ICD, characterized by several DAMPs such as surface CRT translocation and the extracellular release of soluble mediators in GBM cells.

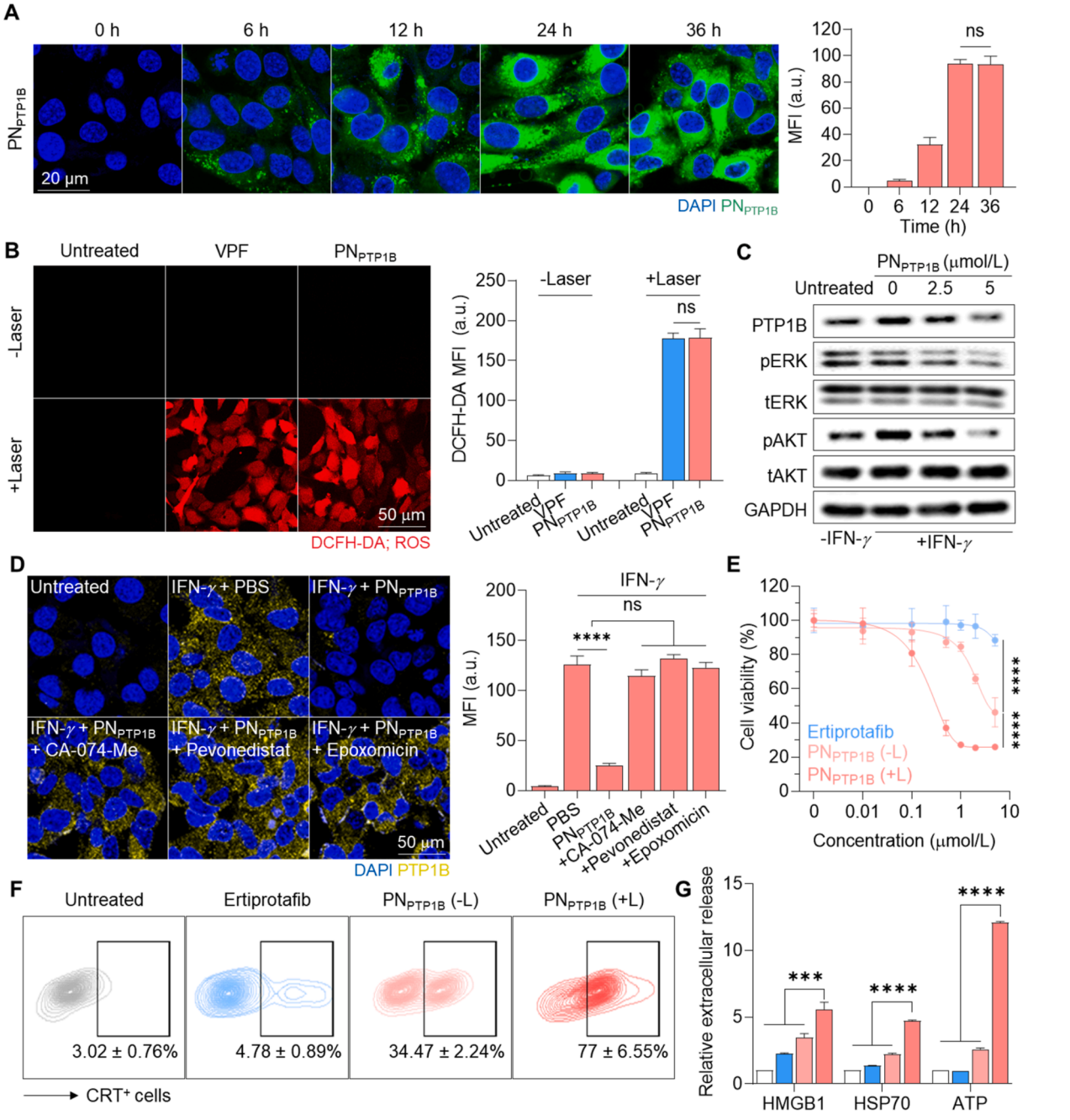


Figure 2 Photodynamic PTP1B proteolysis in GBM cells. (A) Representative fluorescence images of GL261 cells after treatment with PN_{PTP1B} ($n = 3$). (B) ROS generation in GL261 cells following treatment with VPF or PN_{PTP1B} in the absence (-L) or presence (+L) of laser irradiation ($n = 3$). (C) Expression levels of PTP1B and proteins related to the Src/ERK and PI3K/AKT pathways in GL261 cells incubated with the indicated treatments. (D) Representative fluorescence images of PTP1B-stained GL261 cells after incubation with the indicated treatments ($n = 3$). (E) GL261 cell viability following treatment with ertiprotafib or PN_{PTP1B} (-L or + L; $n = 5$). 0 μmol/L PN_{PTP1B} (+L) represents the viability of GL261 cells exposed to the laser without PN_{PTP1B} treatment. (F) Surface CRT expression and (G) extracellular release of HMGB1, HSP70 and ATP in GL261 cells following treatment with ertiprotafib or PN_{PTP1B} (-L or + L; $n = 3$). Data are expressed as mean ± SD. $^{***}P < 0.001$, $^{****}P < 0.0001$.

3.3. *T cell reinvigoration by PTP1B proteolysis*

Next, we investigated the beneficial effects of PTP1B proteolysis in T cells, given the crucial role of PTP1B as an intracellular immune checkpoint associated with T cell exhaustion[8]. PTP1B expression was significantly upregulated in $CD8^+$ T cells isolated from tumor tissues of GL261 tumor-bearing mice relative to splenic T cells from tumor models and naive mice (Fig. 3A). Consequently, T cells in tumors exhibited a high proportion of exhaustion markers PD-1 and Tim3 (Fig. 3B). This illustrates that T cell exhaustion occurs due to an immunosuppressive network consisting of cancer cells, stromal cells, inflammatory cells and

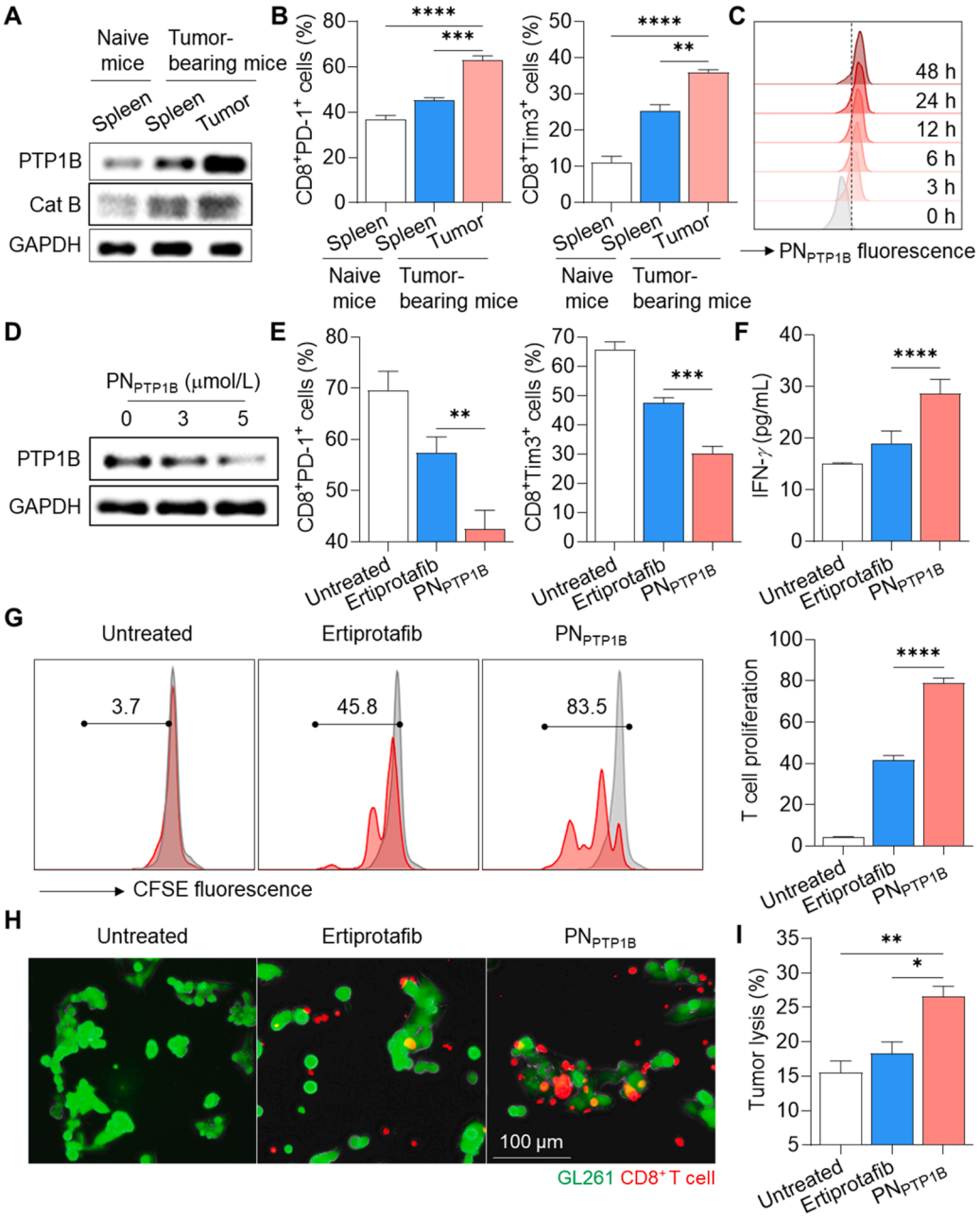


Figure 3 T cell reinvigoration by PTP1B proteolysis. (A) Expression levels of PTP1B and cathepsin B (Cat B) in splenic and tumor-derived T cells from GL261 tumor-bearing mice, as well as splenic T cells from naive mice. (B) Populations of PD-1-positive and Tim3-positive cells within T cells isolated from different origins ($n = 3$). (C) Time-dependent cellular uptake of PN_{PTP1B} in tumor-derived T cells. (D) Expression levels of PTP1B in tumor-derived T cells after treatment with PN_{PTP1B}. (E) Populations of PD-1-positive and Tim3-positive cells within tumor-derived T cells treated with ertiprotafib or PN_{PTP1B} ($n = 3$). (F) Extracellular IFN-γ release from tumor-derived T cells treated with ertiprotafib or PN_{PTP1B} ($n = 3$). (G) Proliferation of tumor-derived T cells treated with ertiprotafib or PN_{PTP1B} ($n = 3$). (H) Representative fluorescence images of GL261 cells cocultured with tumor-derived T cells treated with ertiprotafib or PN_{PTP1B}. (I) Lysis of GL261 cells by tumor-derived T cells treated with ertiprotafib or PN_{PTP1B} ($n = 3$). Data are expressed as mean ± SD. $^*P < 0.05$, $^{**}P < 0.01$, $^{***}P < 0.001$, $^{****}P < 0.0001$.

cytokines in the tumor microenvironment[2]. We also found that intratumoral T cells expressed higher levels of Cat B compared to splenic T cells from tumor-bearing and naive mice. Based on these results, we postulated that PN_{PTP1B} could lead to the activation and proliferation of TILs by alleviating exhaustion through PTP1B proteolysis, thereby enhancing their effector function.

PN_{PTP1B} showed similar cellular uptake in intratumoral T cells as in GBM cells, with maximum accumulation 24 h post-incubation, leading to the degradation of intracellular PTP1B (Fig. 3C and D, Supporting Information Fig. S13). Importantly, 48 h of treatment with nanoassemblies significantly down-regulated PD-1 (42.47 ± 6.41%) and Tim3 (30.2 ± 4.33%) expression levels compared to the untreated (PD-1: 69.6 ± 6.46%, Tim3: 65.6 ± 4.84%) or ertiprotafib-treated (PD-1: 57.43 ± 5.29%, Tim3: 47.53 ± 3.11%) groups (Fig. 3E and Supporting Information Fig. S14). We further analyzed the

exhaustion markers 24 h-post treatment. T cells treated with ertiprotafib or PN_{PTP1B} showed lower PD-1 and Tim3 levels compared to untreated cells, though no significant differences were observed between the two groups (Supporting Information Fig. S15). These results highlight the continuous target protein degradation by PN_{PTP1B} due to its recyclable action, in stark contrast to ertiprotafib, which is effective but not sustained. PTP1B proteolysis mediated by PN_{PTP1B} subsequently initiated T cell activation, as evidenced by a higher quantity of extracellular release of the inflammatory cytokine IFN-γ (Fig. 3F). Ultimately, extensive proliferation was observed in T cells following treatment with PN_{PTP1B} rather than ertiprotafib (Fig. 3G). These effects resulted in a significant number of PN_{PTP1B}-treated T cells surrounding the GBM cells in the coculture system, suggesting enhanced recognition of the target cells (Fig. 3H). Finally, GL261 cell lysis by cocultured T cells significantly increased in the PN_{PTP1B} group relative to the other groups (Fig. 3I). These findings underscore the remarkable effect of nanoassemblies in reinvigorating T cells *via* PTP1B degradation.

3.4. *In vivo antitumor immune responses by photodynamic PTP1B proteolysis*

The *in vivo* efficacy of PN_{PTP1B}-mediated photodynamic PTP1B proteolysis was evaluated in GBM mouse models established by subcutaneous inoculation of GL261 cells into the flanks. Initially, near-infrared fluorescence (NIRF) imaging was conducted to track biodistribution and determine the optimal timing for laser irradiation. As shown in Supporting Information Fig. S16A, PN_{PTP1B} demonstrated outstanding tumor targeting due to passive accumulation *via* the EPR effect in contrast to the small molecule VPF, which exhibited poor tumor targetability[44]. *Ex vivo* NIRF images further confirmed their significant tumor accumulation 3 h post-injection (Fig. S16B). Based on these results, both compounds with an equivalent VPF dose were intravenously injected into mice, followed by laser irradiation on the GBM tissues 3 h after treatment. Therapeutic efficacy was assessed in five groups: (i) Saline, (ii) Laser only (Laser), (iii) PROTAC (Supporting Information Fig. S17), (iv) VPF with laser (+L), (v) PN_{PTP1B} without

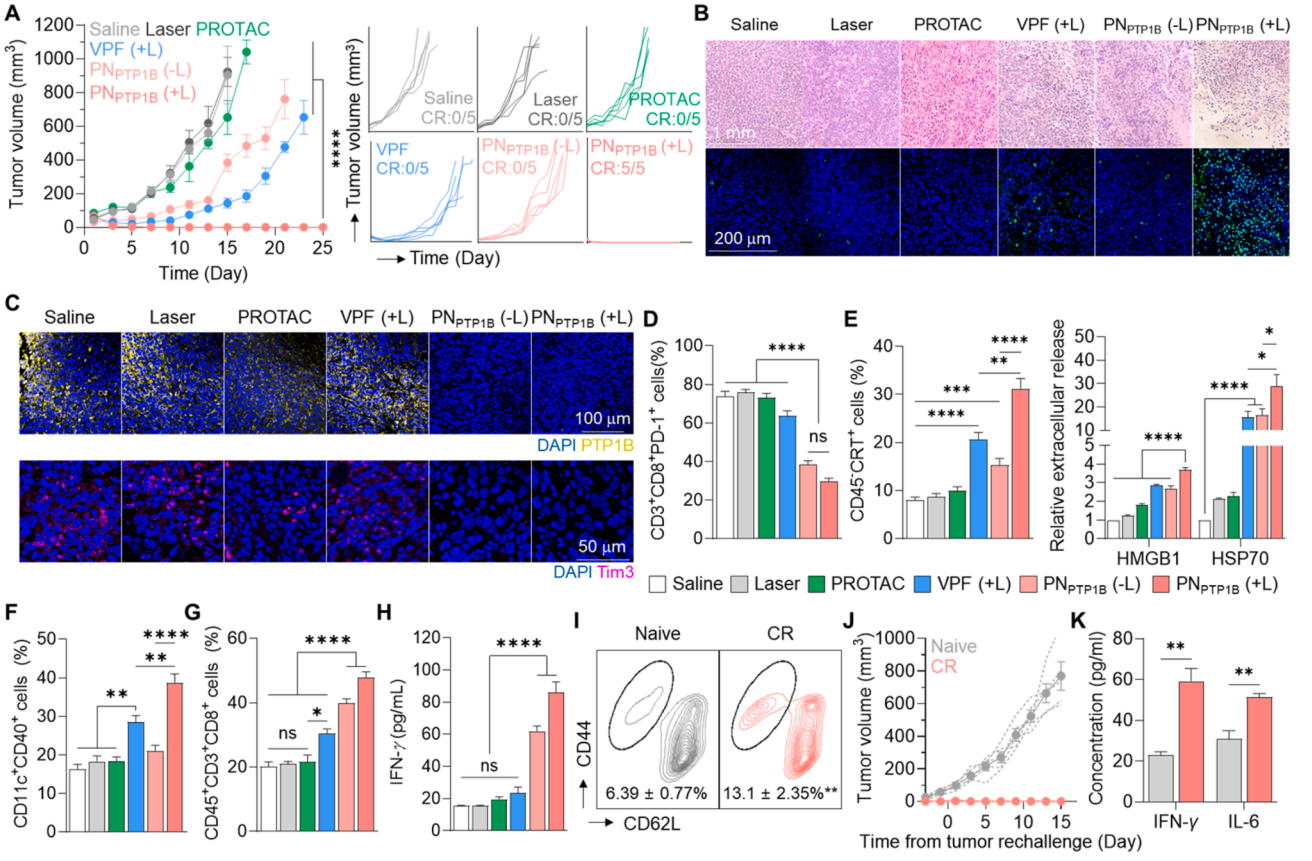


Figure 4 Antitumor immune responses induced by photodynamic PTP1B proteolysis in a GBM model. (A) GL261 tumor growth in mice following treatment with saline, laser only (Laser), PROTAC, VPF with laser irradiation (+L), PN_{PTP1B} without laser irradiation (-L) or PN_{PTP1B} (+L; $n = 5$). (B) GBM tissues stained with H&E and TUNEL. (C) Representative fluorescence images of tumor tissues stained for PTP1B or Tim3. (D) Population of PD-1-positive T cells in tumor tissues ($n = 5$). (E) Population of CRT-positive tumor cells and relative extracellular levels of HMGB1 and HSP70 in GBM tissues ($n = 5$). Populations of (F) mature DCs and (G) cytotoxic T cells in tumor tissues ($n = 5$). (H) Level of IFN-γ in tumor supernatants ($n = 5$). (I) Population of splenic effector/memory T cells in CR and naive mice following GL261 tumor rechallenge ($n = 5$). (J) Rechallenged GL261 tumor growth in CR and naive mice, with dashed lines showing individual tumor growth ($n = 5$). (K) Serum levels of IFN-γ and IL-6 in CR and naive mice following tumor rechallenge ($n = 5$). Data are expressed as mean ± SD. $^*P < 0.05$, $^{**}P < 0.01$, $^{***}P < 0.001$, $^{****}P < 0.0001$.

laser (-L) and (vi) PN_{PTP1B} (+L). While the other groups showed constant tumor progression, all mice in the PN_{PTP1B} (+L) group experienced complete regression (CR) within 8 days of treatment (Fig. 4A). Histological analysis revealed marked structural abnormalities and apoptosis in tumor tissues from the PN_{PTP1B} (+L) group (Fig. 4B and Supporting Information Fig. S18). Meanwhile, no noticeable changes in body weight or damage to major organs were observed in any of the groups during the 25 days following treatment (Supporting Information Fig. S19).

The antitumor immune response was evaluated by examining changes in tumor immunogenicity on Day 3 following treatment using the same protocol as above. Treatment with either PN_{PTP1B} (-L) or (+L) significantly reduced the expression levels of PTP1B and Tim3 in tumor tissues in comparison to the other groups (Fig. 4C and Supporting Information Fig. S20). This indicates the restoration of exhausted TILs through *in vivo* PTP1B degradation by PN_{PTP1B}'s PROTAC activity. The effects of nanoassemblies in reinvigorating T cell function in tumor tissues were further confirmed by a decrease in PD-1-positive T cells ($CD3^+CD8^+PD\text{-}1^+$) in both the PN_{PTP1B} (-L) and (+L) groups (Fig. 4D and Supporting Information Fig. S21). Next, the tumor tissues from the PN_{PTP1B} (+L) group exhibited a significantly increased population of CRT-positive tumor cells ($CD45^-CRT^+$) compared to the VPF (+L) and PN_{PTP1B} (-L) groups. These results, along with a substantial extracellular release of HMGB1 and HSP70, were associated with DC maturation, characterized by the presence of $CD11c^+CD40^+$ cells in tumor tissues (Fig. 4E and F, Supporting Information Fig. S22). Consequently, the PN_{PTP1B} (+L) group showed a 1.2-fold increase in cytotoxic T cells in tumor tissues relative to the PN_{PTP1B} (-L) group (Fig. 4G and Supporting Information Fig. S23). The enhanced activity of TILs in the PN_{PTP1B} (+L) group was verified by their substantial release of IFN-γ into tumor supernatants (Fig. 4H). Note that the population and function of TILs also increased in the PN_{PTP1B} (-L) groups due to PTP1B inhibition-mediated T cell activation. Given that PDT could damage T cells, the apoptosis rate of T cells within tumor tissues was assessed, showing no significant differences between the VPF (+L)

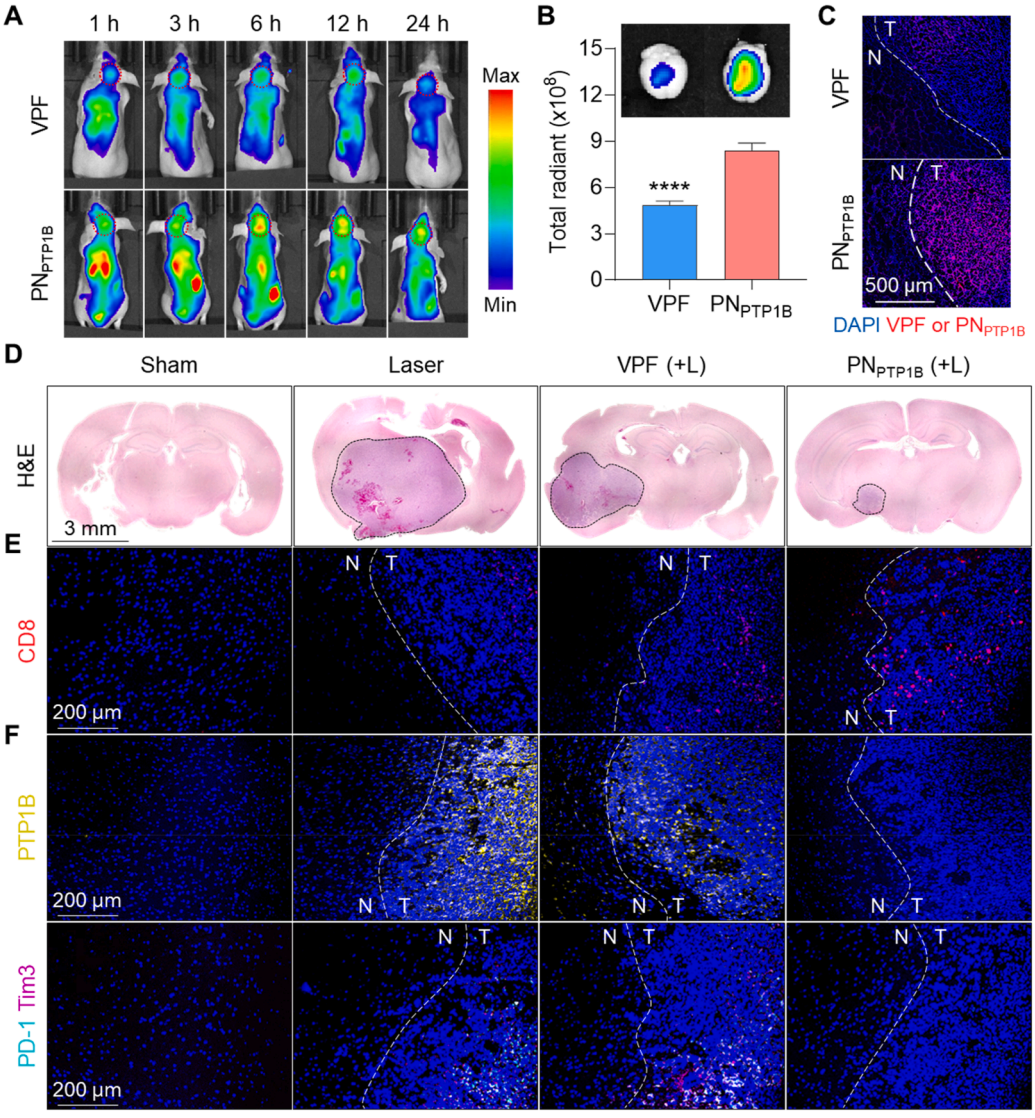


Figure 5 Therapeutic efficacy of photodynamic PTP1B proteolysis in an orthotopic GBM model. (A) Whole-body NIRF images of orthotopic GBM mice after intravenous injection of VPF or PN_{PTP1B}. Red circles indicate the region of the orthotopic GBM. (B) *Ex vivo* NIRF images of GBM tissues 6 h after administration of VPF or PN_{PTP1B} ($n = 3$). (C) Histology showing GBM accumulation of VPF and PN_{PTP1B}. (D) GBM tissues stained with H&E on Day 10 following treatment. GBM tissues stained for (E) CD8, (F) PTP1B, or PD-1 and Tim3. 'N' and 'T' in the Figures indicate the non-tumor and tumor regions, respectively. Data type? Data are expressed as mean ± SD. $^{****}P < 0.0001$.

and PN_{PTP1B} (+L) groups compared to the saline group (Supporting Information Fig. S24). This is because tumor tissues initially show a low population of T cells, with infiltration beginning after laser irradiation for PDT-induced ICD. Taken together, these findings highlight the unique mechanism of nanoassemblies in combining PDT and PTP1B proteolysis to induce potent ICD in tumors and reverse the immunosuppressive tumor microenvironment. Meanwhile, T cells are not exposed to PDT, as they reach the tumor tissues after ICD. Subsequently, T cells overexpress cathepsin B due to priming and activation in response to released DAMPs and tumor antigens, primarily undergoing PTP1B degradation and alleviating exhaustion.

Afterward, the mice that experienced CR due to treatment with PN_{PTP1B} (+L) were rechallenged with GBM cells to assess the immunological memory conferring resistance against recurrence by previously encountered tumors. As expected, a hallmark of adaptive immunity after cancer immunization, the proportion of effector memory T cells (T_{em}) within splenic $CD8^+$ T cells increased considerably in CR mice as opposed to naive mice (Fig. 4I). This resulted in protective immune responses, with rechallenged GL261 cells failing to grow in CR mice (Fig. 4J). Furthermore, the serum levels of IL-6 and IFN-γ were significantly upregulated in the CR mice in comparison to naive mice on Day 15 post-tumor rechallenge (Fig. 4K).

3.5. *Therapeutic efficacy of photodynamic PTP1B proteolysis in a GBM orthotopic model*

The efficacy of PN_{PTP1B} was further assessed in the GBM orthotopic model. We first monitored the biodistribution of nanoassemblies in the orthotopic model using NIRF imaging to optimize the timing of laser irradiation (Fig. 5A and Supporting Information Fig. S25). The fluorescence from PN_{PTP1B} observed in the brain was higher than that of VPF, exhibiting a 2.16-fold greater intensity at 6 h post-injection at which both reached peak accumulation. This is attributable to the commonly observed phenomenon that nanoparticles penetrate the disrupted BBB during GBM progression[23]. *Ex vivo* NIRF imaging further confirmed the considerable presence of nanoassemblies in the brain tissues (Fig. 5B). Particularly, histological analysis visualized a substantial accumulation of PN_{PTP1B} in the tumor regions within the brains (Fig. 5C and Supporting Information Fig. S26). When the tumor regions were exposed to laser irradiation 6 h after administration, PN_{PTP1B} suppressed GBM formation and growth more effectively than VPF (Fig. 5D and Supporting Information Fig. S27). Orthotopic tumor tissues in the PN_{PTP1B} (+L) group revealed a significantly higher quantity of effector T cells compared to the other groups (Fig. 5E and Supporting Information Fig. S28). These results are attributed to the downregulation of PD-1 and Tim3 in the GBM region due to effective PTP1B proteolysis by PN_{PTP1B} (+L) treatment (Fig. 5F and Supporting Information Fig. S29). Consequently, extensive apoptotic cell death occurred within the GBM area following treatment with PN_{PTP1B} (+L) (Supporting Information Fig. S30). Taken together, our findings emphasize the remarkable efficacy of PN_{PTP1B}'s photodynamic PTP1B proteolysis for effectively eradicating GBM.

4. Conclusions

In summary, we established a streamlined yet effectively coordinated nanomedicine to elicit an innate immune response and eliminate T cell exhaustion for countering ITM within GBM. By leveraging PROTAC technology, removing intracellular PTP1B resulted in obvious effects depending on the cell types. In tumor cells, PTP1B degradation amplified the ICD induced by PDT under laser irradiation, which promoted DC maturation and T cell priming. On the other hand, intratumoral T cells experienced downregulation of PD-1 and Tim3 due to PTP1B knockdown, counteracting T cell exhaustion caused by the immunosuppressive network in GBM and continuously maintaining their functionality. To maximize the efficacy of these events, nanoassemblies integrating a photosensitizer and PTP1B-targeting PROTAC were designed to cross the disrupted BBB and reach the desired region. Furthermore, these two distinct therapeutics were linked with a substrate peptide for the GBM biomarker cathepsin B, enabling selective activation at the target site while minimizing uncontrolled off-target proteolysis by PROTAC. Particularly, with the supramolecular assembly mechanism, the nanomedicine developed in this study represented innovative advancements from both technical and industrial perspectives by excluding the need for excessive carrier materials used in conventional nanoparticles. Given that this system could be extended to other POIs by incorporating relevant targeting moieties, this study offers a versatile platform for photodynamic proteolysis, inspiring further research into the broader application of PROTACs in cancer immunotherapy. By combining with recent advanced medical devices, such as optical fibers and implantable devices, the efficacy and safety of PROTAC nanoassemblies for GBM treatment can be further enhanced by overcoming the fundamental shortcoming of light's limited penetration depth through precise and efficient light delivery to deeper tumor regions.

Acknowledgments

This work was supported by grants from the National Research Foundation (NRF) of Korea, funded by the Ministry of Science (RS-2025-02219039, RS-2021-NR061836, RS-2024-00343156, NRF-2022R1A2C2006861, RS-2024-00463774, RS-2022-NR068161 and RS-2024-00405287) and the Intramural Research Program of KIST.

Author contributions

Yeongji Jang: investigation, methodology, formal analysis, data curation, writing-original Draft. Jiwoong Choi: validation, formal analysis, investigation, data curation, visualization. Byeongmin Park: methodology, investigation. Jung Yeon Park: methodology, investigation. Jae-Hyeon Lee: methodology, investigation. Jagyeong Goo: Investigation. Dongwon Shin: investigation. Sun Hwa Kim: investigation. Yongju Kim: investigation. Hyun Kyu Song: investigation. Jooho Park: investigation. Kwangmeyung Kim: resources, funding acquisition, supervision, writing-Original Draft. Yoosoo Yang: resources, supervision, funding acquisition, project administration, writing-original draft. Man Kyu Shim: conceptualization, methodology, resources, supervision, funding acquisition, project administration, writing-original draft.

Conflicts of interest

The authors declare that they have no known competing financial interests or personal relationships that could have appeared to influence the work reported in this paper.

Appendix A. Supporting information

Supporting information to this article can be found online at https://doi.org/10.1016/j.apsb.2025.06.028.

References

1. Schaff LR, Mellinghoff IK. Glioblastoma and other primary brain malignancies in adults: a review. *JAMA* 2023;**329**:574−87.
2. Jackson CM, Choi J, Lim M. Mechanisms of immunotherapy resistance: lessons from glioblastoma. *Nat Immunol* 2019;**20**: 1100−9.
3. DeCordova S, Shastri A, Tsolaki AG, Yasmin H, Klein L, Singh SK, et al. Molecular heterogeneity and immunosuppressive microenvironment in glioblastoma. *Front Immunol* 2020;**11**:1402.
4. Dumas AA, Pomella N, Rosser G, Guglielmi L, Vinel C, Millner TO, et al. Microglia promote glioblastoma *via* mTOR-mediated immunosuppression of the tumour microenvironment. *EMBO J* 2020;**39**: e103790.
5. Ravi VM, Neidert N, Will P, Joseph K, Maier JP, Kückelhaus J, et al. T-cell dysfunction in the glioblastoma microenvironment is mediated by myeloid cells releasing interleukin-10. *Nat Commun* 2022;**13**:925.
6. Liang S, Tran E, Du X, Dong J, Sudholz H, Chen H, et al. A small molecule inhibitor of PTP1B and PTPN2 enhances T cell anti-tumor immunity. *Nat Commun* 2023;**14**:4524.
7. Jin T, Li D, Yang T, Liu F, Kong J, Zhou Y. PTPN1 promotes the progression of glioma by activating the MAPK/ERK and PI3K/AKT pathways and is associated with poor patient survival. *Oncol Rep* 2019;**42**:717−25.
8. Wiede F, Lu KH, Du X, Zeissig MN, Xu R, Goh PK, et al. PTP1B is an intracellular checkpoint that limits T-cell and CAR T-cell antitumor immunity. *Cancer Discov* 2022;**12**:752−73.
9. Delibegović M, Dall'Angelo S, Dekeryte R. Protein tyrosine phosphatase 1B in metabolic diseases and drug development. *Nat Rev Endocrinol* 2024;**20**:366−78.
10. Békés M, Langley DR, Crews CM. PROTAC targeted protein degraders: the past is prologue. *Nat Rev Drug Discov* 2022;**21**:181−200.
11. Li K, Crews CM. PROTACs: past, present and future. *Chem Soc Rev* 2022;**51**:5214−36.
12. Garber K. The PROTAC gold rush. *Nat Biotechnol* 2022;**40**: 12−6.
13. Schott AF, Hurvitz S, Ma C, Hamilton E, Nanda R, Zahrah G, et al. Abstract GS3-03: GS3-03 ARV-471, a PROTAC® estrogen receptor (ER) degrader in advanced ER-positive/human epidermal growth factor receptor 2 (HER2)-negative breast cancer: phase 2 expansion (VERITAC) of a phase 1/2 study. *Cancer Res* 2023;**83**:GS3-03-GS3-03.
14. Dong J, Miao J, Miao Y, Qu Z, Zhang S, Zhu P, et al. Small molecule degraders of protein tyrosine phosphatase 1B and T-cell protein tyrosine phosphatase for cancer immunotherapy. *Angew Chem Int Ed* 2023;**62**:e202303818.
15. Zhang C, Zeng Z, Cui D, He S, Jiang Y, Li J, et al. Semiconducting polymer nano-PROTACs for activatable photo-immunometabolic cancer therapy. *Nat Commun* 2021;**12**:2934.
16. Li G, Sun B, Li Y, Luo C, He Z, Sun J. Small-molecule prodrug nanoassemblies: an emerging nanoplatform for anticancer drug delivery. *Small* 2021;**17**:2101460.
17. Moon Y, Cho H, Kim J, Song S, Yeon Park J, Young Min J, et al. Self-assembled peptide-derived proteolysis-targeting chimera (PROTAC) nanoparticles for tumor-targeted and durable PD-L1 degradation in cancer immunotherapy. *Angew Chem Int Ed* 2025;**64**:e202414146.
18. Park B, Han G, Jin DY, Gil KC, Shin D, Lee J, et al. Mucoadhesive mesalamine prodrug nanoassemblies to target intestinal macrophages for the treatment of inflammatory bowel disease. *ACS Nano* 2024;**18**: 16297−311.
19. Kyu Shim M, Yang S, Sun IC, Kim K. Tumor-activated carrier-free prodrug nanoparticles for targeted cancer Immunotherapy: preclinical evidence for safe and effective drug delivery. *Adv Drug Deliv Rev* 2022;**183**:114177.
20. Park B, Kim EH, Jang H, Kim Y, Ryu Y, Choi J, et al. Drug repositioning of mesalamine *via* supramolecular nanoassembly for the treatment of drug-induced acute liver failure. *Theranostics* 2025;**15**: 1122−34.
21. Sharifi S, Reuel N, Kallmyer N, Sun E, Landry MP, Mahmoudi M. The issue of reliability and repeatability of analytical measurement in industrial and academic nanomedicine. *ACS Nano* 2022;**17**:4−11.
22. Jiang S, Li W, Yang J, Zhang T, Zhang Y, Xu L, et al. Cathepsin B-responsive programmed brain targeted delivery system for chemo-immunotherapy combination therapy of glioblastoma. *ACS Nano* 2024;**18**:6445−62.
23. Wolburg H, Noell S, Fallier-Becker P, Mack AF, Wolburg-Buchholz K. The disturbed blood−brain barrier in human glioblastoma. *Mol Aspect Med* 2012;**33**:579−89.
24. Lim SH, Yee GT, Khang D. Nanoparticle-based combinational strategies for overcoming the blood-brain barrier and blood-tumor barrier. *Int J Nanomed* 2024:2529−52.
25. Tran VL, Lux F, Tournier N, Jego B, Maître X, Anisorac M, et al. Quantitative tissue pharmacokinetics and EPR effect of AGuIX nanoparticles: a multimodal imaging study in an orthotopic glioblastoma rat model and healthy macaque. *Adv Healthcare Mater* 2021;**10**: 2100656.
26. Caro C, Avasthi A, Paez-Muñoz JM, Leal MP, García-Martín ML. Passive targeting of high-grade gliomas *via* the EPR effect: a closed path for metallic nanoparticles? *Biomater Sci* 2021;**9**:7984−95.
27. Jeon S, Jun E, Chang H, Yhee JY, Koh EY, Kim Y, et al. Prediction the clinical EPR effect of nanoparticles in patient-derived xenograft models. *J Control Release* 2022;**351**:37−49.
28. Wang B, Hu S, Teng Y, Chen J, Wang H, Xu Y, et al. Current advance of nanotechnology in diagnosis and treatment for malignant tumors. *Signal Transduct Targeted Ther* 2024;**9**:200.
29. Xu Q, Wu N, Li X, Guo C, Li C, Jiang B, et al. Inhibition of PTP1B blocks pancreatic cancer progression by targeting the PKM2/AMPK/mTOC1 pathway. *Cell Death Dis* 2019;**10**:874.
30. Chen Y, Wang L, Chen N, Tang G. Metformin induces tumor immunogenic cell death in ovarian cancer by activating AMPK pathway. *Transl Oncol* 2024;**47**:102052.
31. Mondesir J, Ghisi M, Poillet L, Bossong RA, Kepp O, Kroemer G, et al. AMPK activation induces immunogenic cell death in AML. *Blood Adv* 2023;**7**:7585−96.
32. Ma M, Jiang W, Zhou R. DAMPs and DAMP-sensing receptors in inflammation and diseases. *Immunity* 2024;**57**:752−71.
33. Zheng ZY, Lin W, Su JW, Huang QF, Zhang C, Pan WX, et al. NIR-715 photodynamic therapy induces immunogenic cancer cell death by enhancing the endoplasmic reticulum stress response. *Cell Death Dis* 2024;**15**:890.
34. Wang Q, Li S, Xu C, Wang X, Yang T, Wang C, et al. Glutaminolysis inhibition boosts photodynamic therapy to eliminate cancer stem cells. *Biomaterials* 2024;**306**:122497.
35. Wang Z, Fan X, Mu G, Zhao X, Wang Q, Wang J, et al. Cathepsin B-activatable cyclic antisense oligonucleotides for cell-specific target gene knockdown *in vitro* and *in vivo*. *Mol Ther Nucleic Acids* 2023;**33**: 548−58.
36. Kim J, Song S, Gwak M, Cho H, Yun WS, Hwang N, et al. Micro-syringe chip-guided intratumoral administration of lipid nanoparticles for targeted anticancer therapy. *Biomater Res* 2023; **27**:102.
37. Liu JZ, Zhang SE, Nie F, Yang Y, Tang YB, Yin W, et al. Discovery of novel PTP1B inhibitors *via* pharmacophore-oriented scaffold hopping from Ertiprotafib. *Bioorg Med Chem Lett* 2013; **23**:6217−22.
38. Min Jh, Yang H, Ivan M, Gertler F, Kaelin Jr WG, Pavletich NP. Structure of an HIF-1α-pVHL complex: hydroxyproline recognition in signaling. *Science* 2002;**296**:1886−9.

39. Kim HS, Seo M, Park TE, Lee DY. A novel therapeutic strategy of multimodal nanoconjugates for state-of-the-art brain tumor phototherapy. *J Nanobiotechnol* 2022;**20**:14.
40. Shim MK, Yoon HY, Ryu JH, Koo H, Lee S, Park JH, et al. Cathepsin B-specific metabolic precursor for *in vivo* tumor-specific fluorescence imaging. *Angew Chem Int Ed* 2016;**55**:14698−703.
41. Sirks MJ, van Dijk EH, Rosenberg N, Hollak CE, Aslanis S, Cheung CMG, et al. Clinical impact of the worldwide shortage of verteporfin (Visudyne®) on ophthalmic care. *Acta Ophthalmol* 2022; **100**:e1522−32.
42. Choi J, Park B, Park JY, Shin D, Lee S, Yoon HY, et al. Light-triggered PROTAC nanoassemblies for photodynamic Ido proteolysis in cancer immunotherapy. *Adv Mater* 2024;**36**:2405475.
43. Singh S, Grewal AS, Grover R, Sharma N, Chopra B, Dhingra AK, et al. Recent updates on development of protein-tyrosine phosphatase 1B inhibitors for treatment of diabetes, obesity and related disorders. *Bioorg Chem* 2022;**121**:105626.
44. Fang J, Islam W, Maeda H. Exploiting the dynamics of the EPR effect and strategies to improve the therapeutic effects of nanomedicines by using EPR effect enhancers. *Adv Drug Deliv Rev* 2020;**157**:142−60.